ISSN 0915-633X

NATIONAL INSTITUTE FOR FUSION SCIENCE

Recent Experiments on Li Pellet Injection into Heliotron E

V.Yu. Sergeev, K.V. Khlopenkov, B.V. Kuteev, S. Sudo, K. Kondo, F. Sano, H. Zushi, H. Okada, S. Besshou, T. Mizuuchi, K. Nagasaki, Y. Kurimoto and T. Obiki

(Received - June 27, 1996)

NIFS-428 Aug. 1996

RESEARCH REPORT
NIFS Series

NAGOYA, JAPAN

Recent Experiments on Li Pellet Injection into Heliotron E

V Yu Sergeev, K V Khlopenkov and B V Kuteev

State Technical University, Polytekhnicheskaya 29, St. Petersburg, 195251 Russia

S Sudo

National Institute for Fusion Science, Nagoya, 464-01 Japan

K Kondo, F. Sano, H Zushi, H Okada, S Besshou, T Mizuuchi, K Nagasaki, Y Kurimoto and T Obiki

Plasma Physics Laboratory, Kyoto University, Kyoto, 611 Japan

Abstract

The Li pellets of a large size were injected into ECR heated plasmas and NBI heated plasmas of Heliotron E The discharge behavior, pellet ablation and wall conditioning were studied The electron pressure is doubled after injection into NBI plasma and unchanged in case of ECR heating This may be caused by the energy exchange between electrons, thermal ions with fast ions from the neutral beam The observed discrepancy between the experimental and modeled ablation rates may be explained by both the plasma cooling by pellet ablatant and ablation stimulated with the fast ions during NBI heated regime and fast electrons during ECR heated regime. In the preliminary experiments on wall conditioning by Li pellet injection, no improvement of plasma performance after Li pellet injection was observed in both divertor configuration and limiter configuration with the limiter radii r_L = 24-25 cm.

Key Words lithium pellet injection, Heliotron E, lithium pellet ablation, impurity particle behavior, wall conditioning

1. Introduction.

Experiments with pellet injection in general and impurity pellet injection in particular are very important since there are a useful tool for plasma diagnostics. In case of Li pellet injection it is possible to observe behavior of the Li clouds and to calculate the ablation rate of the pellet. Such calculations were performed in the experiments on TFTR for Ohmically heated discharges and supershots [1]. An improvement of the plasma performance after injection of a fairly large (∅ 2×2 mm size) cylindrical Li pellet has been observed on TFTR as well [2]. In case of the helical magnetic configuration experiments with injection of Li pellets were carried out in order to: (1) study a response of the main plasma parameters during the injection and a possible change in global plasma confinement due to injection, (2) study the ablation properties of Li pellet injected into ECR and NBI heated currentless plasma, (3) study effect of plasma conditioning by lithium coating on the wall

2. Experimental setup.

The schematic diagram of Li pellet injection experiments on Heliotron E is shown in Fig. 1. The new Li pellet injector described in Ref. [3] was used. The pellet injection axis laid in the equatorial plane of the machine and had the angle equal to 8 degrees relative to the major radius direction. The optical system with a set of half-transparent mirrors (HM) was used to measure a pellet ablation process.

The emission of Li pellet clouds was observed from outward direction using optical fiber (1) and two photomultiplyers equipped with two light filters (LF) with following parameters: the wave lengths λ and the widths $\Delta\lambda$ were $\lambda_I = 670.9$ nm, $\Delta\lambda = 1.1$ nm and $\lambda_{II} = 548.5$ nm, $\Delta\lambda = 1.5$ nm respectively. This allowed us to measure the pellet cloud emission lines of neutrals (*LiI*, $\lambda = 670.6$ nm) and first ions (*LiII*, $\lambda = 548.5$ nm) of lithium. Optical fiber (1) had a wide view angle which was restricted by elements of the construction. As a result we could measure

the different dimensions of clouds along the pellet trace ~5 cm at the outward direction boundary of the vacuum vessel, ~7-8 cm in the vicinity of the vacuum vessel axis and about of 10 cm at the inward direction boundary of the vacuum vessel Three optical channels equipped by optical fibers (2-4) with a set of both lenses and light filters (LF) had a narrow view angle in the radial direction (~ 2-3 cm view dimension in the vicinity of the vacuum vessel axis) and were installed in order to connect the time of pellet flight with its space positions

Pellet clouds were measured from inward direction using optical fiber (5), light filter and either the CCD camera or the high speed camera with quickly moving film (up to $4 \cdot 10^4$ frames/sec) The level of emission through both filters for *LiI*, *LiII* lines drastically decreased in the high speed camera (due to a small exposure time - 25-50 μs) so that we saw a few frames with pellet clouds which corresponded to maximum of the pellet ablation rate The obtained experience of the intensities level should help us to improve further measurements using both cameras.

3. Experimental results and discussion.

The cylindrical pellets with size of ∅1 mm×1 mm and with velocities in a range of 400–500 m/s were injected into the Heliotron E plasmas The injection was performed into three types of discharges: ECR heated plasma (by a 106 GHz, 350 kW gyrotron), NBI heated plasma (by 23 kV, 3 5 MW neutral beams), and NBI+ECR simultaneously heated plasma. The magnetic field strength was 1 9 T The vacuum chamber wall was boronized by ECR discharge with $B_{10}H_{14}$ and He [4] The plasma response and pellet ablation were observed to be similar in the NBI and NBI+ECR regimes and quite differ out from those observed in the ECR heated plasma. It seems that this difference occurs due to significantly different values of ECR (350 kW) and NBI (3.5 MW) powers Therefore, we omit (NBI+ECR) data and present here the data obtained for two type of regimes - NBI and ECR heated plasma

3.1 Plasma response on Li pellet injection.

Behavior of the main plasma parameters in the typical discharges for two types of regimes are shown in Fig. 2a,b Each plot includes a signal $\bar{n}_e l$ of the FIR interferometer (a linear integral of the electron density along the central chord in the poloidal cross section); an ECE signal corresponding to the central electron temperature; a wide view bolometer signal; the powers of ECR and NBI heatings; transverse plasma energy $<W_\perp>$ measured by plasma diamagnetism and Boron emission (BIV). The moments of pellet injection are shown by vertical arrows in Fig. 2a,b. The dashed curves represent an evolution of the parameters without pellet injection. We see that Li pellet deposition (electron density rise $\Delta(\bar{n}_e l) = 2.2 \cdot 10^{15}$ cm^{-2} in shot #70597) in the NBI regime is about of two times higher than in the ECR regime ($\Delta(\bar{n}_e l) = 1.0 \cdot 10^{15}$ cm^{-2} n shot #70667). It seems that a behavior of electron temperature measured by ECE diagnostics after pellet injection shown in Fig. 2a,b might be not correct because the ECE signal from the central region could be damped due to the cut-off conditions that appears when the density exceeds values about of 10^{14} cm^{-3} This suspicion was confirmed by measurements of electron density and temperature by means of the Thomson Scattering (TS) technique (see below). We see no significant rise of the total radiation after pellet injection. It is seen a rise of $<W_\perp>$ signal immediately after pellet injection in the NBI regime The rise of $<W_\perp>$ signal in the ECR regime can not be detected but we see that the Li pellet injection leads to increase the plasma energy content during the following evolution when the NBI power switches on. (See Fig. 2b.).

Estimations based on the electron density rise $\Delta(\bar{n}_e l)$ (similar those made for TFTR data [1]) show that at the Heliotron E plasma conditions a Li pellet with ∅1 mm × 1 mm size (total number of atoms in the pellet is $3.6 \cdot 10^{19}$) deposits in the plasma about of 30% of its mass in case of the ECR heated plasma and about of 60% in case of NBI regime. For example, the last value for the NBI regime we estimated by means of both calculated values $\Delta(\bar{n}_e l) = 2.05 \cdot 10^{15}$ cm^{-2} (using the emission signal I_{LiI}) and $\Delta(\bar{n}_e l) = 2.35 \cdot 10^{15}$ cm^{-2} (using the emission

signal I_{LiII}) in shot #70597 what corresponds to the experimental value $\Delta(n_e l) = 2\,2 \cdot 10^{15}$ cm^{-2} measured in this shot

These estimations of Li pellet deposition are confirmed by measurements of density profiles using the TS technique Changes of electron density, temperature and pressure profiles due to Li injection measured by the TS in two types of regimes are shown in Fig. 3a,b These plots include the data obtained in several discharges and represent general response of the parameters in similar plasma conditions. The profiles were measured before the injection (open squares in Fig 3) and 4–6 ms after (crosses) The range of measurement times after pellet injection appeared because the time of TS's laser pulse was fixed while the time of pellet ablation could vary due to slightly different velocities of pellet which had to fly the long distance of about 5.5 m between the exit of the injector barrel and plasma It is seen that after the injection the electron pressure increases about two times in the NBI regime (the central electron temperature changes from 0 75 keV to 0 5 keV and the central density from $5 \cdot 10^{13}$ cm^{-3} to $15 \cdot 10^{13}$ cm^{-3}) A similar comparison in case of ECR discharges (the central electron temperature changes from 1 5 keV to 0 5 keV and the central density from $3 \cdot 10^{13}$ cm^{-3} to $9 \cdot 10^{13}$ cm^{-3}) shows that the plasma response is almost adiabatic, with conservation of the electron pressure

The temporal evolution of the central, averaged values of ion temperature $\langle T_i \rangle$ measured using the neutral particle analyzer (NPA) and the transverse plasma energy $\langle W_\perp \rangle$ deduced from the diamagnetic measurements (DIA) are shown in Fig 4 for the NBI regime. We evaluated the ratio of the transversal plasma energy $\langle W_\perp \rangle$ before pellet injection $\langle W_{\perp 1} \rangle$ (for $t_1 = 327$ ms) to one $\langle W_{\perp 2} \rangle$ after injection (for $t_2 = 333$ ms) These time moments are marked by dashed vertical lines in Fig 4 Because this experimental value $\langle W_{\perp 2} \rangle / \langle W_{\perp 1} \rangle$ = 8 2/5 6 ~ 1 5 less than the ratio $P_{e2} / P_{e1} \approx 2$ measured by TS technique (see Fig 3a), we tried to make a self-consistent explanation of all (TS, NPA and DIA) measurements using the simple following speculations Let us assume that the normalized T_e $T_e(0)$ and T_i $T_i(0)$ profiles are the same just before and 4-6 ms after pellet injection Then, we can estimate the ratio of the

transversal plasma energy $<W_{\perp}>$ before pellet injection $<W_{\perp 1}>$ to one $<W_{\perp 2}>$ after injection using the changes of the core values of electron and ion temperatures

$$\frac{<W_{\perp 2}>}{<W_{\perp 1}>} = \frac{\int_0^a \left[n_{e2}(r)T_{e2}(r) - n_{i2}(r)T_{e2}(r)\frac{T_{i2}(0)}{T_{e2}(0)} \right] rdr}{\int_0^a \left[n_{e1}(r)T_{e1}(r) - n_{i1}(r)T_{i1}(r)\frac{T_{i1}(0)}{T_{e1}(0)} \right] rdr}$$

From Fig. 3a, 4a we can take the following values of $T_{e1}(0) = 0.7$ keV, $T_{e2}(0) = 0.4$ keV, $T_{i1}(0) = 0.55$ keV, $T_{i2}(0) = 0.4$ keV. Here, $n_{e1}(r) = n_{i1}(r)$, $n_{i2}(r) = n_{e1}(r) + (n_{e2}(r) - n_{e1}(r))/Z_{Li}$, where $Z_{Li} = 3$ is nuclear charge of lithium and $a = 30$ cm is a radius of the last closed magnetic surface The calculated value of the ratio $<W_{\perp 2}>/<W_{\perp 1}> = 9/5.3 \sim 1\ 7$ is no far from the experimental value $<W_{\perp 2}>/<W_{\perp 1}> \sim 1.5$ obtained from Fig. 4b if we take into account accuracy of this estimation..

The increase of electron pressure after injection into NBI heated plasma may have the following explanation. A source of such a heating of electrons after the injection may come from the fast ions of the neutral beam. First of all, the absolute power deposition of NBI is increased due to the increased both density and charge state Z. Then, the critical beam energy of the fast ions is lowered by a factor of 0 57 (for $Z_{Li}=3$ and $A_{Li}=7$) which results in a more favorable heating of the electrons. For a further detailed analysis we should take into account the interactions: (a) electrons – fast ions H^+, (b) thermal ions Li^{+++} and D^+ – fast ions H^+.

3.2 Ablation studies.

The typical signals of the intensities I_{LiI}, I_{LiII} and the chord-averaged electron density measured in two types of regime are shown in Fig. 5,6. First of all, we see that start of I_{LiI}, I_{LiII} signals (see Fig. 4a and Fig. 5a) are delayed (~1 ms) relative to the time of the density rise that is impossible. The reason of that is connected with a difference of sampling frequencies of

time basis of the independent data acquisition systems, which were used for measurements of intensities and electron density

The process of pellet-plasma interaction can be divided in three stages (I,II,III) which are separated by vertical dashed lines in Fig 5,6 During the first stage the pellet goes through the hot region of the plasma Then pellet enters in the cold region behind the inner last closed magnetic surface (LCMS) (stage II) situated at the major radius of about 190 cm The third stage (III) begins after pellet impacts with the inner wall surface situated at 180 cm. Knowing the pellet velocity values we adjusted the radial dependence of the I_{LiI}, I_{LiII} signals in each type of regimes relative to the electron temperature profiles $T_{e0}(r)$ which were fitted to those measured using TS technique before pellet injection (see Fig 3). The result of such procedure is shown in Fig 5b and Fig. 6b The values of major radii for the magnetic axis $R_c = 218$ cm, the inner LCMS $R^{in}_{LCMS} = 188$ cm and for the outer LCMS $R^{out}_{LCMS} = 248$ cm were taken from calculations of the plasma equilibrium for the studied magnetic configuration of the Heliotron E plasma [5] We assumed that the ablation starts in the vicinity of the region with electron temperature values of about 50 eV. Thus, the ablation starts at radii $R^{NBI}_{st} \approx 245$ cm (in Fig. 5b) and $R^{ECR}_{st} \approx 241$ cm (in Fig. 6b). It is seen from Fig 5,6 that signal I_{LiII} finished in the end of the first stage while signal I_{LiI} grows in the end of the first stage, during the second stage and decays in third stage Maybe it is because the pellet cloud temperature decreased when pellet passed through the magnetic axis and faced to the ambient plasma with lowered electron temperature values.

It is not clear what emission profile ($I_{LiI}(r)$ or $I_{LiII}(r)$) could represent better a behavior of the Li pellet ablation rate Therefore, the ablation rate profiles $\dot{N}_{LiI,LiII}(r)$ deduced using both signals were calculated and they are shown in Fig 7a and Fig 8a for two types of regime The values of the total deposition of electrons due to pellet injection $N_e \approx 6 \cdot 10^{19}$ (for the NBI regime) and $N_e \approx 3 \cdot 10^{19}$ (for the ECR regime) were used to normalize the $I_{LiI}(r)$, $I_{LiII}(r)$ signals. These N_e values were calculated using the approximation of the electron density profiles $n_{e1}(r)$ and $n_{e0}(r)$ fitted to ones measured by means of the TS technique before and after

Li pellet injection (see Fig. 3). For $I_{LiI}(t)$ signals lasted 4-5 ms we can make it because the electron density increases during a time interval about of 1 ms (see Fig. 4a and Fig. 5a).

The obtained $\dot{N}_{LiI,LiII}(r)$ profiles are compared with those simulated using the neutral shielding model by Kuteev *et al.* for impurity Li pellet [6,7] in Fig. 7a,8a We can see a moderate difference in $\dot{N}_{LiI,LiII}(r)$ profiles and an apparent discrepancy between experimental ablation rate profiles and the modeled $\dot{N}_{mod}(r)$ profile. Discrepancy in the plasma core and in the inner part of the plasma column can be understood because the model by Kuteev *et al* does not take into account plasma cooling by the ablatant that was evaporated earlier as well.

We have improved the ablation model taking into account the self-limiting phenomenon as described below We used the expression for the ablation rate values given by Kuteev *et al.* for calculations of the ablation rate profile in the outward part of plasma column. For each step of calculations on minor radius $r_{i-1} = r_i + \Delta r$ we estimated the disturbed values of electron density $n_{e1}(r_{i-1}) = n_{e0}(r_{i-1}) + \Delta n_e(r_{i-1})$ and temperature $T_{e1}(r_{i-1}) = T_{e0}(r_{i-1}) - \Delta T_e(r_{i-1})$ The perturbation of the electron density $\Delta n_e(r_{i-1})$ was calculated using the ablation rate $\dot{N}(r_{i-1})$

$$\Delta n_e(r_{i+1}) = \frac{\dot{N}(r_{i+1})Z_{Li}}{2\pi R_C 2\pi V_p r_i \dot{k}_{elong}}$$

and electron temperature was allowed to decrease adiabatically ($n_{e1}(r_{i-1})\ T_{e1}(r_{i-1}) = n_{e0}(r_{i-1})\ T_{e0}(r_{i-1})$) with the cold electrons added Here, $k_{elong} \approx 2$ is elongation factor of the plasma column. Then, we used the expression for the ablation rate values given by Kuteev *et al* for calculations of the ablation rate profile in the inward part of plasma column using the disturbed profiles $T_{e1}(r)$, $n_{e1}(r)$. The results of the simulations by means of this self-limiting model are shown by dashed-dotted lines in Fig 7a, 8a. We see that the self-limiting model more adequately predicts the ablation rate decreases as the pellet passes the central region of the plasma column in case of ECR regime. For the NBI regime, the enhancement of the measured ablation rate values are larger.

The enhanced ablation rate values in the edge plasma region might be connected with ablating by fast ions during the strong NBI pulse (nearby the inner and outer regions in Fig. 7a)

or with fast electron population during the ECR pulse (nearby the outer region in Fig 8a) which were not taken into account by the used pellet ablation model Let us to note that in experiments on hydrogen pellet injection into Heliotron E plasmas [8], the similar enhanced evaporation of pellet due to both fast ions and electrons was observed as well

The profiles of the ratio $\dot{N}_{LiI}(r)$ $\dot{N}_{LiII}(r)$ shown in Fig 7b and Fig 8b may demonstrate evolution of pellet cloud parameters during the pellet motion and ablation in both types of regimes A possible reason for decrease of this ratio in regions with R 208 cm in Fig 7b (NBI regime) and with R 218 cm in Fig 8b (ECR regime) may be due to the low values of the pellet cloud temperature while pellet goes through the magnetic axis as mentioned above In any case, the numeric simulation of pellet cloud parameters such as cloud density, temperature and I_{LiI}, I_{LiII} emissions are required to make more conclusive statements.

3 3 Experiments on wall conditioning to improve plasma performance.

Relatively large size of Li pellet allowed us to consider the problem of the plasma–wall interaction related to the lithium coating on the wall We studied the NBI regime in which the largest Li pellet deposition was measured (see Fig 2a) To check the possible improvement of the plasma purity, Oxygen V line was observed In Fig 9 signals of OV in two sequential discharges are compared It is seen from this picture that the OV emission at the timing t=305 ms in shot #70705 is almost two times less than that of the before-injection case in shot #70704 However, drawing shot by shot sequence of electron density, impurity content OV, ion temperature $<T_i>$ and plasma energy $<W_p>$ in Fig 10, we do not see any evidence of improvement of plasma performance (enhancement of a stored plasma energy, ion temperature, energy confinement time, plasma purity etc.) as was observed in the Li pellet experiments on TFTR [2] Behavior of these signals was the same as in the case no Li pellet injection into the divertor configuration of Heliotron E We made experiments with inserted limiter configuration expecting more intensive interaction of the Li ablatant with the limiter which had 400x40 mm rectangular cross-section Shot by shot behavior of some plasma parameters in the limiter

configuration is shown in Fig. 11 We see either drop or jump on the signal evolutions when the limiter radius value was decreased from $r_L = 25$ cm to $r_L = 24$ cm but no improvement of plasma performance was observed as well. We hope that the further Li pellet experiments on Heliotron E with $r_L \approx 15$-18 cm can make clear weather improvement of plasma parameters is possible in Heliotron E after injection of large Li pellets or it corresponds to peculiarity of the TFTR experiments (for instance, due to the influence of bump-limiter configuration on TFTR [2])

4. Conclusions.

The Li pellets of a large size were injected into ECR heated plasmas and NBI heated plasmas of Heliotron E. The discharge behavior, pellet ablation and wall conditioning were studied. The electron pressure is doubled after injection into NBI plasma and unchanged in case of ECR heating This may be caused by the energy exchange between electrons, thermal ions with fast ions from the neutral beam. The observed discrepancy between the experimental and modeled ablation rates may be explained by both the plasma cooling by pellet ablatant and ablation stimulated with the fast ions during NBI heated regime and fast electrons during ECR heated regime In the preliminary experiments on wall conditioning by Li pellet injection, no improvement of plasma performance after Li pellet injection was observed in both divertor configuration and limiter configuration with the limiter radii $r_L = 24$-25 cm.

Acknowledgments

The authors are grateful to all personnel of the Heliotron E who helped in these experiments. Especially we would like to thank K. Sakamoto, S. Kado and from NIFS S. Mizusawa. This work was supported by the grant № 10026 of Daiko Foundation.

References

[1] V Yu Sergeev *et al* Lithium pellet deposition and penetration in TFTR, Rev Sci Instrum **63** (1992), 4984-4986

[2] J Snipes *et al* Wall conditioning by lithium pellet injection on TFTR Proc 18th Europ Conf. on Contr Fus and Plasma Phys., Berlin, 3-7 June 1991, part III, III-141

[3] K V Khlopenkov, S Sudo, V. Yu Sergeev Li pellet injector for Heliotron E NIFS Report NIFS-TECH-4 (1996)

[4] K Kondo, T Mizuuchi *et al* J Nucl Mater **220-222** (1995) 1052

[5] T. Obiki, M. Wakatani, M Sato, S Sudo, et al , Fusion Technology 17 (1990) 101

[6] B V Kuteev, V Yu Sergeev, and L. D Tsendin, Interaction of carbon pellets with a hot plasma, Sov. J Plasma Phys **10**(6) Nov.-Dec 1984

[7] S M Egorov *et al.* Current density profile and electron beam localization measurements using carbon pellet on T-10 Nuclear Fusion **32** (1992) 2025-2028

[8] S Sudo, K. Kondo, H. Zushi, F Sano, in Controlled Fusion and Plasma Physics (Proc. 21th Europ. Conf Montpellier, 1994) 18B (1994) 1546

Figure captions.

Fig. 1. Schematic diagram of experiments on Li pellet injection into Heliotron E.

Fig. 2. Temporal dependencies of the FIR signal of line density at r=2 cm, ECE second harmonic signal of the temperature, signal of the wide view bolometer, input powers of ECR and NBI heating, transverse plasma energy $<W_\perp>$ measured by plasma diamagnetism and Boron (BIV) radiation:

a) NBI regime - Li pellet was injected at t=328 ms in shot #70597 (solid curves) and no injection was in shot #70600 (dotted curves);

b) ECR regime - Li pellet was injected at t=288 ms in shot #70667 (solid curves) and no injection was in shot #70600 (dotted curves);

Fig. 3. Profiles of the electron temperature, density and electron pressure just before (squares) and 4-6 ms after (crosses) the Li injection into NBI (a) and ECR (b) heated plasmas Solid and dashed curves show represent approximations of the data before and after injection respectively. Equations for approximate profiles of electron temperature $T_{e0}(r)$, $T_{e1}(r)$ (in [keV]) and density $n_{e0}(r)$, $n_{e1}(r)$ (in [10^{13} cm^{-3}]) are shown.

Fig. 4 Temporal evolution of the central, averaged values of ion temperature $<T_i>$ measured using the neutral particle analyzer (NPA) and the transversal plasma energy $<W_\perp>$ deduced from the diamagnetic measurements in the NBI regime

Fig. 5.a) Time dependencies of the typical signals of intensities I_{LiI}, I_{LiII} and the line-averaged electron density measured in shot #70597 (NBI regime), b) The radial dependence of the I_{LiI}, I_{LiII} signals shown in Fig. 5a and the electron temperature profiles $T_{e0}(r)$ which is fitted to one measured using TS technique before pellet injection (see Fig.. 2a);

Fig 6 a) Time dependencies of the typical signals of intensities I_{LiI}, I_{LiII} and the line-averaged electron density measured in shot #70667 (ECR regime), b) The radial dependence of the I_{LiI}, I_{LiII} signals shown in Fig 6a and the electron temperature profiles $T_{e0}(r)$ which is fitted to one measured using TS technique before pellet injection (see Fig. 2b),

Fig 7 Li pellet ablation in NBI heated plasma (Shot #70597, pellet velocity is 480 m/s)

a) ablation rate profiles solid curve – measured using the LiII intensity; dotted curve – measured using LiI intensity; dashed curve – calculated using the ablation model by Kuteev *et al* [5,6], dashed-dotted curve - calculated using the self-limiting ablation model

b) ratio of the ablation rate profiles measured using the LiI and LiII intensities,

Fig 8 Li pellet ablation in ECR heated plasma (Shot #70667, pellet velocity is 470 m/s)

a) ablation rate profiles solid curve – measured using the LiII intensity, dotted curve – measured using LiI intensity; dashed curve – calculated using the ablation model by Kuteev *et al.* [5,6], dashed-dotted curve - calculated using the self-limiting ablation model.

b) ratio of the ablation rate profiles measured using the LiI and LiII intensities;

Fig 9 Temporal dependencies of the OV line intensity for two shots #70704 (with Li pellet injection) and #70705 (no pellet injection)

Fig 10. The line-averaged electron density, transverse plasma energy, total plasma radiation, the intensity of OV and BIV lines measured at 322 ms in a series of NBI heated discharges with the divertor configuration (crosses indicate those discharges in which Li pellet was injected at 327-329 ms)

Fig 11. The transverse plasma energy, total plasma radiation, the intensity of CIII (in the vicinity of limiter), OV and BIV lines measured at 332 ms in a series of NBI heated discharges with the limiter configuration (crosses indicate those discharges in which Li pellet was injected at 347-349 ms)

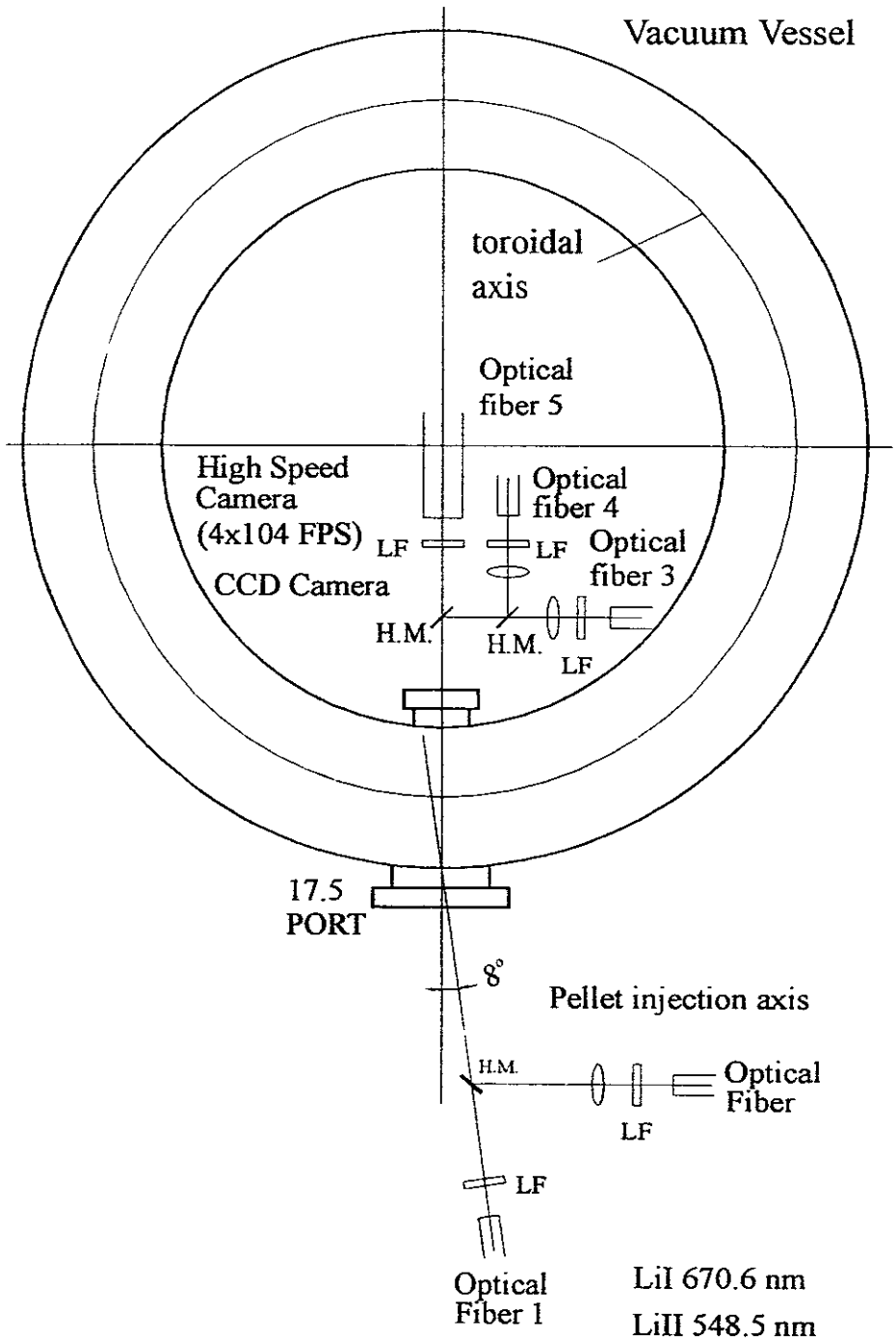
Vacuum Vessel
toroidal
axis
Optical
fiber 5
High Speed
Camera
(4x104 FPS)
CCD Camera
LF
Optical
fiber 4
LF
Optical
fiber 3
H.M.
H.M.
LF
17.5
PORT
8°
Pellet injection axis
H.M.
Optical
Fiber
LF
LF
Optical
Fiber 1
LiI 670.6 nm
LiII 548.5 nm

Fig. 1

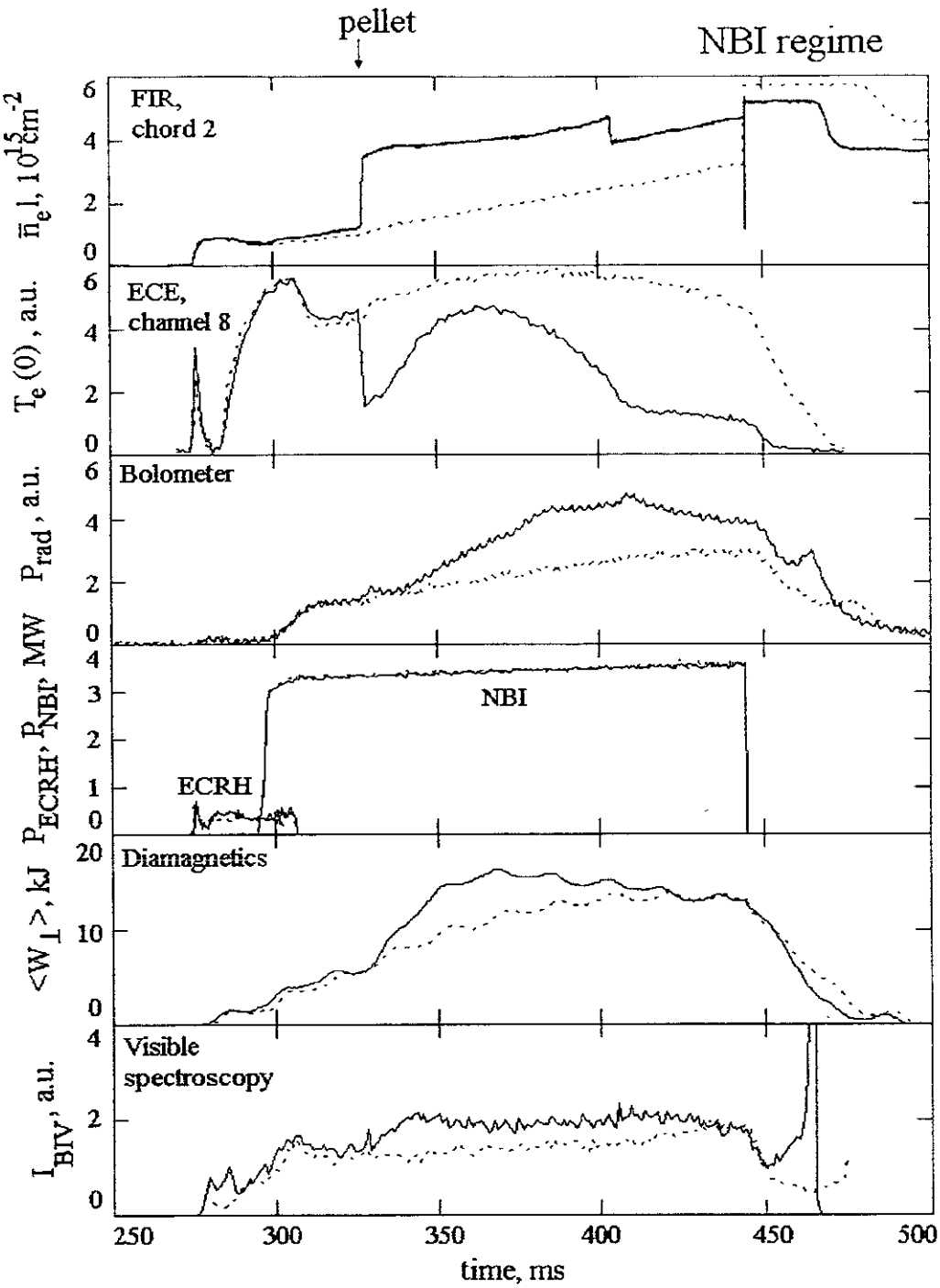
pellet
NBI regime
FIR,
chord 2
$\bar{n}_e l$, 10^{15}cm^{-2}
ECE,
channel 8
$T_e(0)$, a.u.
Bolometer
P_{rad}, a.u.
NBI
ECRH
P_{ECRH}, P_{NBI}, MW
Diamagnetics
$<W_\perp>$, kJ
Visible
spectroscopy
I_{BIV}, a.u.
time, ms

Fig. 2a

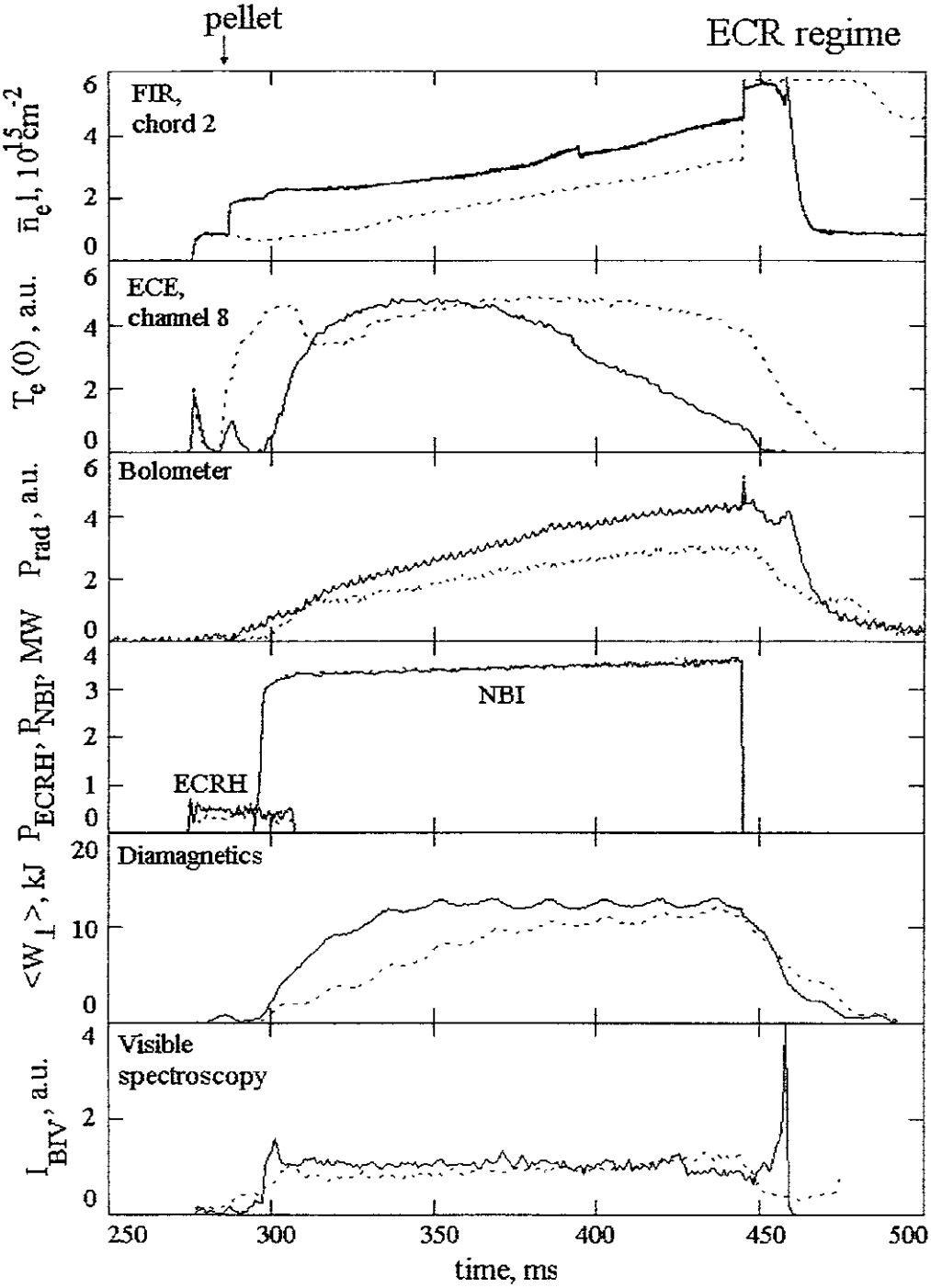
pellet
ECR regime
FIR,
chord 2
$\bar{n}_e l$, 10^{15}cm^{-2}
ECE,
channel 8
$T_e(0)$, a.u.
Bolometer
P_{rad}, a.u.
NBI
ECRH
P_{ECRH}, P_{NBI}, MW
Diamagnetics
$<W_\perp>$, kJ
Visible
spectroscopy
I_{BIV}, a.u.
250
300
350
400
450
500
time, ms

Fig. 2b

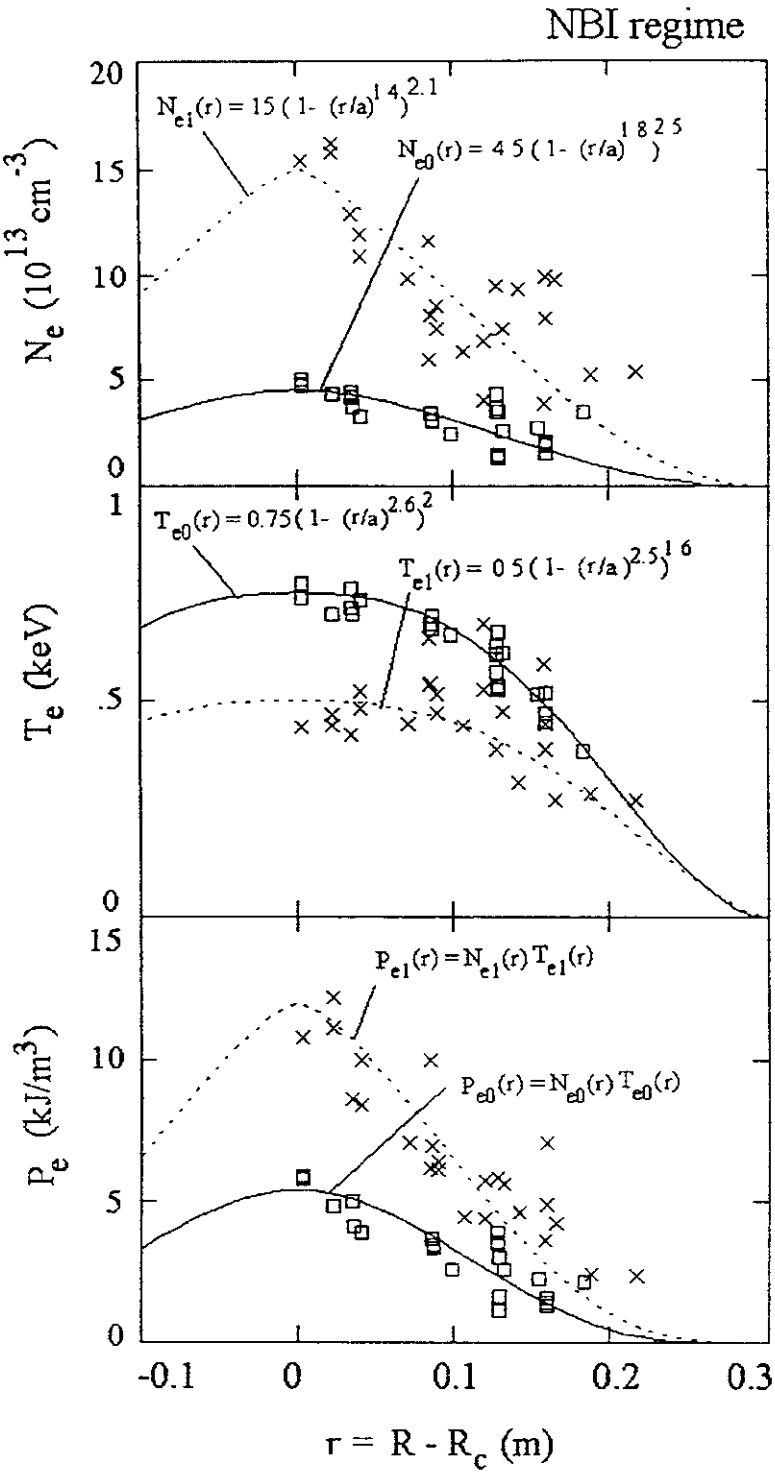
NBI regime
$N_{e1}(r) = 15\,(1 - (r/a)^{14})^{2.1}$
$N_{e0}(r) = 45\,(1 - (r/a)^{18})^{25}$
N_e (10^{13} cm^{-3})
$T_{e0}(r) = 0.75\,(1 - (r/a)^{2.6})^{2}$
$T_{e1}(r) = 05\,(1 - (r/a)^{2.5})^{16}$
T_e (keV)
$P_{e1}(r) = N_{e1}(r)\,T_{e1}(r)$
$P_{e0}(r) = N_{e0}(r)\,T_{e0}(r)$
P_e (kJ/m^3)
r = R - R_c (m)

Fig. 3a

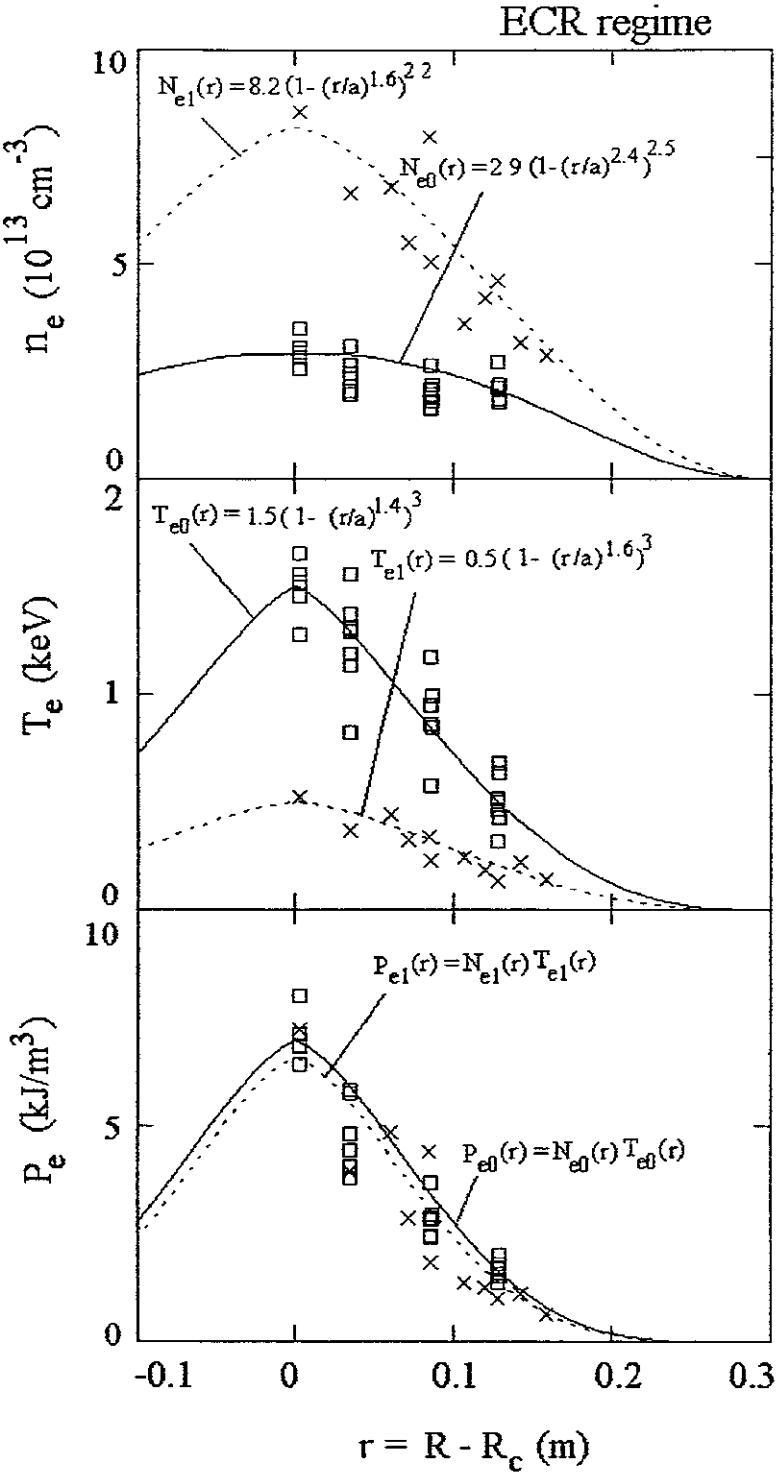
ECR regime
$N_{e1}(r) = 8.2\,(1-(r/a)^{1.6})^{2.2}$
$N_{e0}(r) = 2.9\,(1-(r/a)^{2.4})^{2.5}$
n_e (10^{13} cm^{-3})
$T_{e0}(r) = 1.5\,(1-(r/a)^{1.4})^{3}$
$T_{e1}(r) = 0.5\,(1-(r/a)^{1.6})^{3}$
T_e (keV)
$P_{e1}(r) = N_{e1}(r)\,T_{e1}(r)$
$P_{e0}(r) = N_{e0}(r)\,T_{e0}(r)$
P_e (kJ/m^3)
r = R - R_c (m)

Fig. 3b

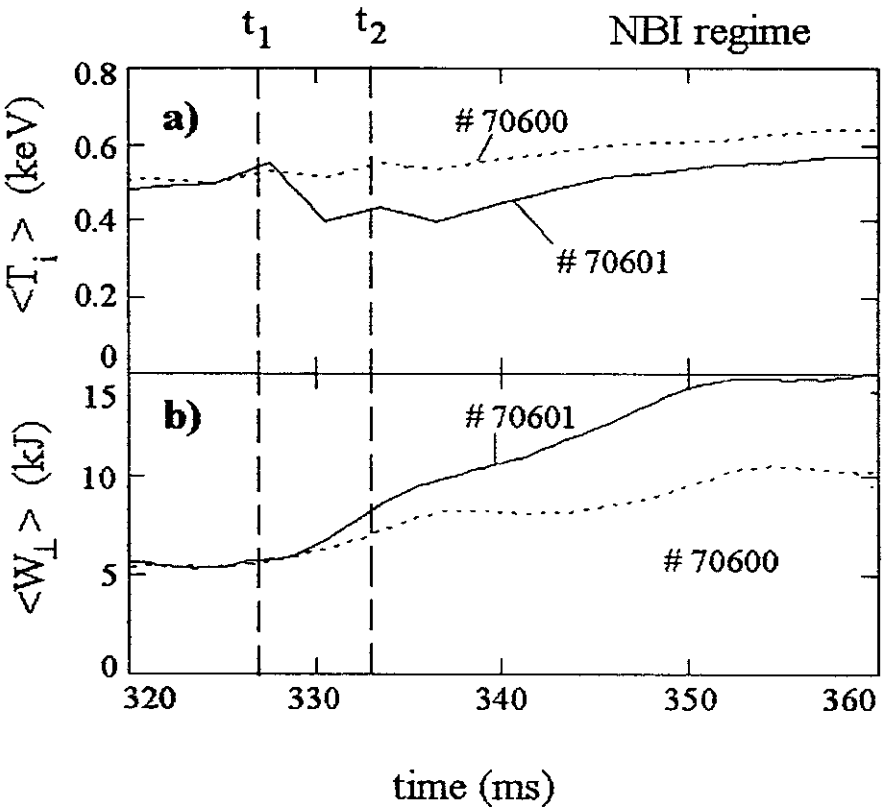
t1
t2
NBI regime
a)
70600
70601
<Ti> (keV)
0.8
0.6
0.4
0.2
0
b)
70601
70600
<W⊥> (kJ)
15
10
5
0
320
330
340
350
360
time (ms)

Fig. 4

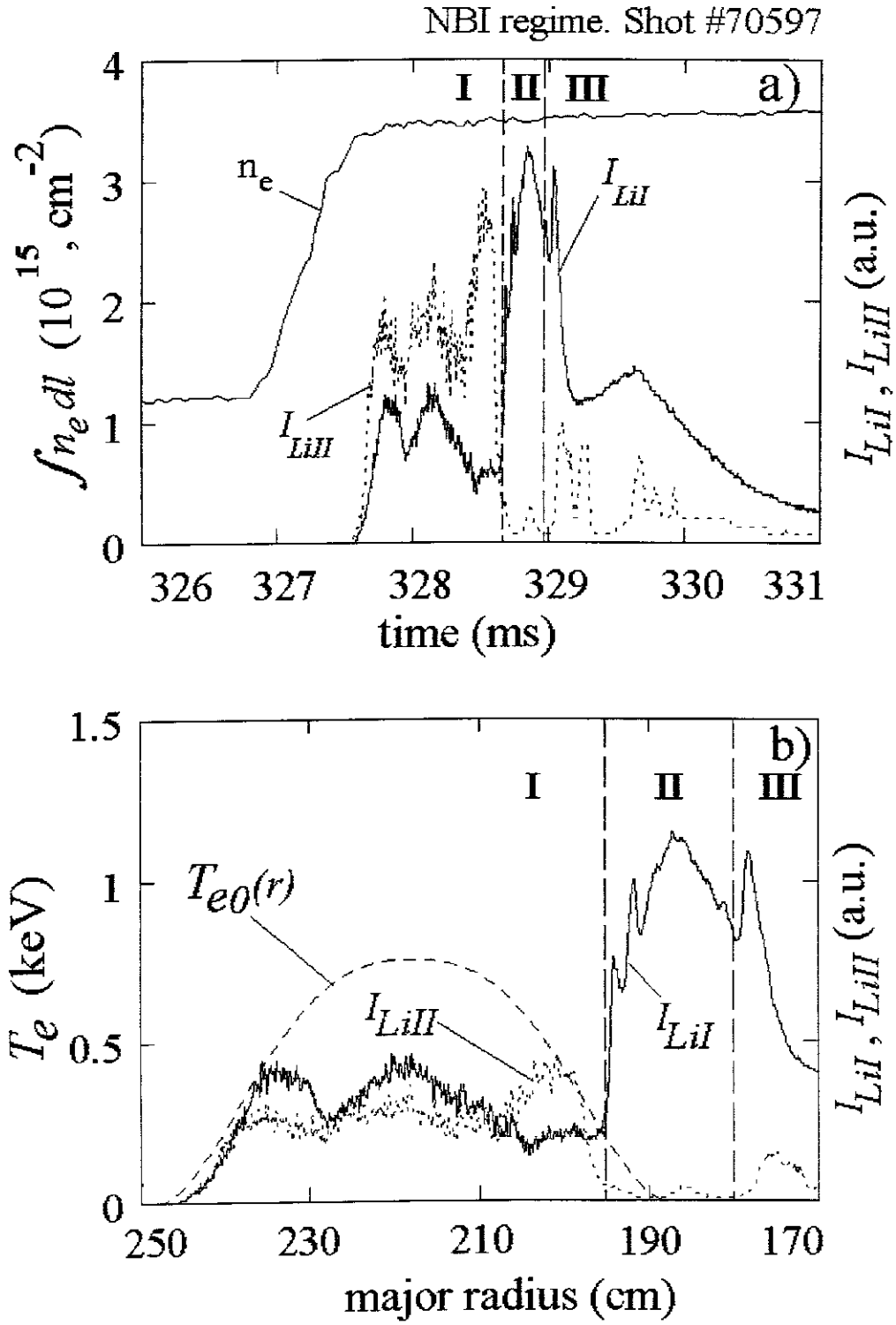
NBI regime. Shot #70597
I
II
III
a)
n_e
I_{LiI}
I_{LiII}
$\int n_e dl$ (10^{15}, cm^{-2})
I_{LiI} , I_{LiII} (a.u.)
time (ms)
b)
$T_{e0(r)}$
T_e (keV)
major radius (cm)

Fig. 5

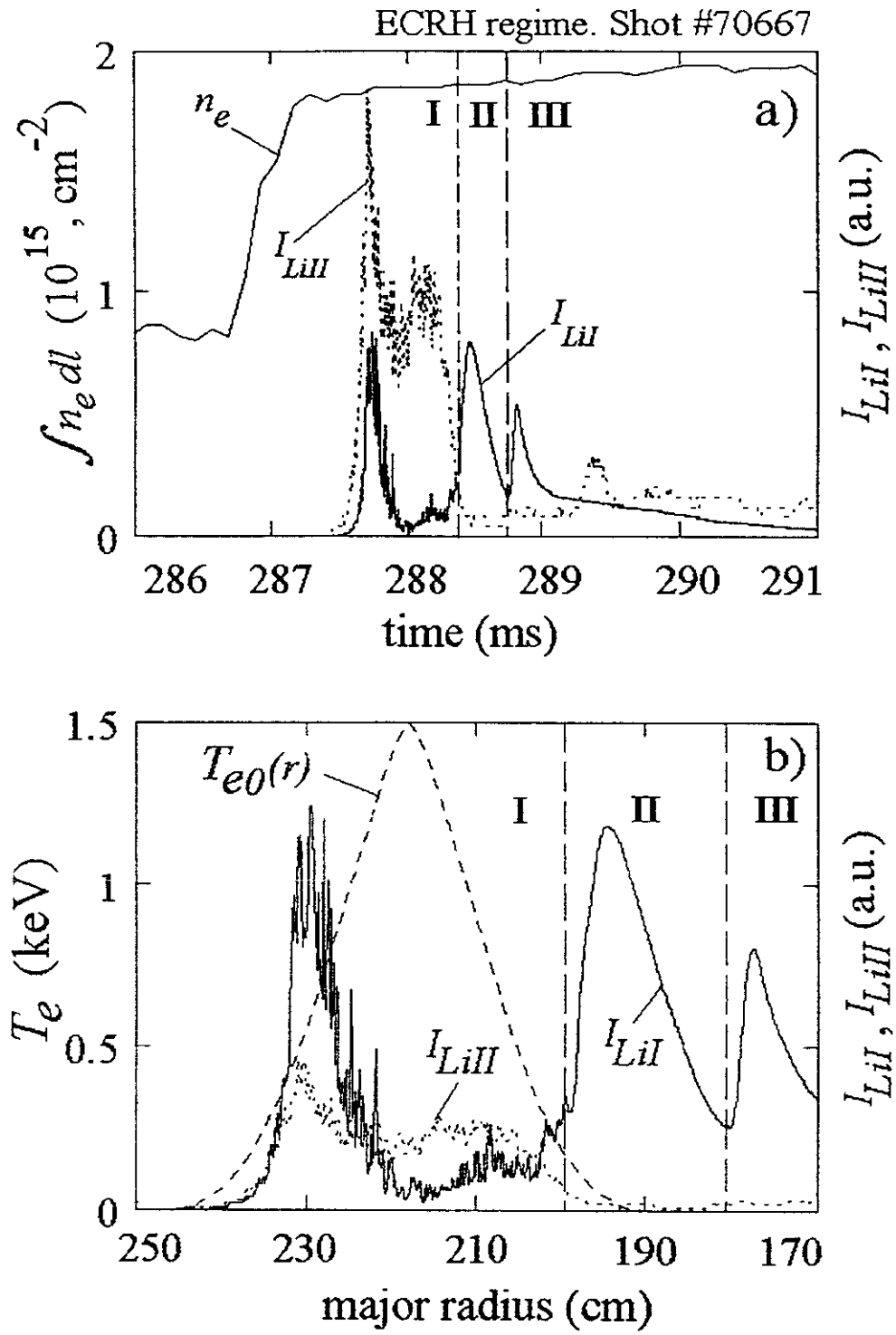
ECRH regime. Shot #70667
a)
n_e
I_{LiII}
I_{LiI}
I
II
III
$\int n_e dl$ (10^{15}, cm^{-2})
I_{LiI}, I_{LiII} (a.u.)
time (ms)
b)
$T_{e0(r)}$
T_e (keV)
major radius (cm)

Fig. 6

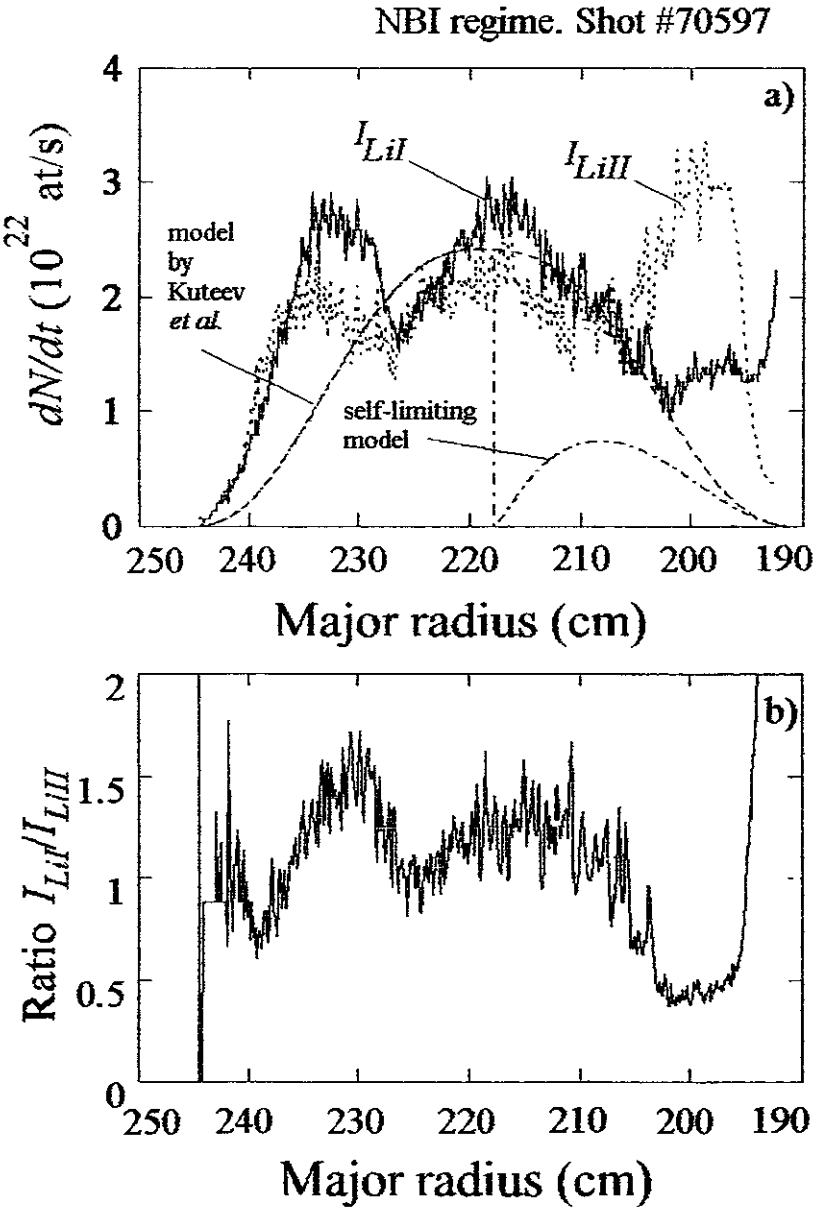
NBI regime. Shot #70597
a)
I_{LiI}
I_{LiII}
model by Kuteev *et al.*
self-limiting model
dN/dt (10^{22} at/s)
Major radius (cm)
b)
Ratio I_{LiI}/I_{LiII}
Major radius (cm)

Fig. 7

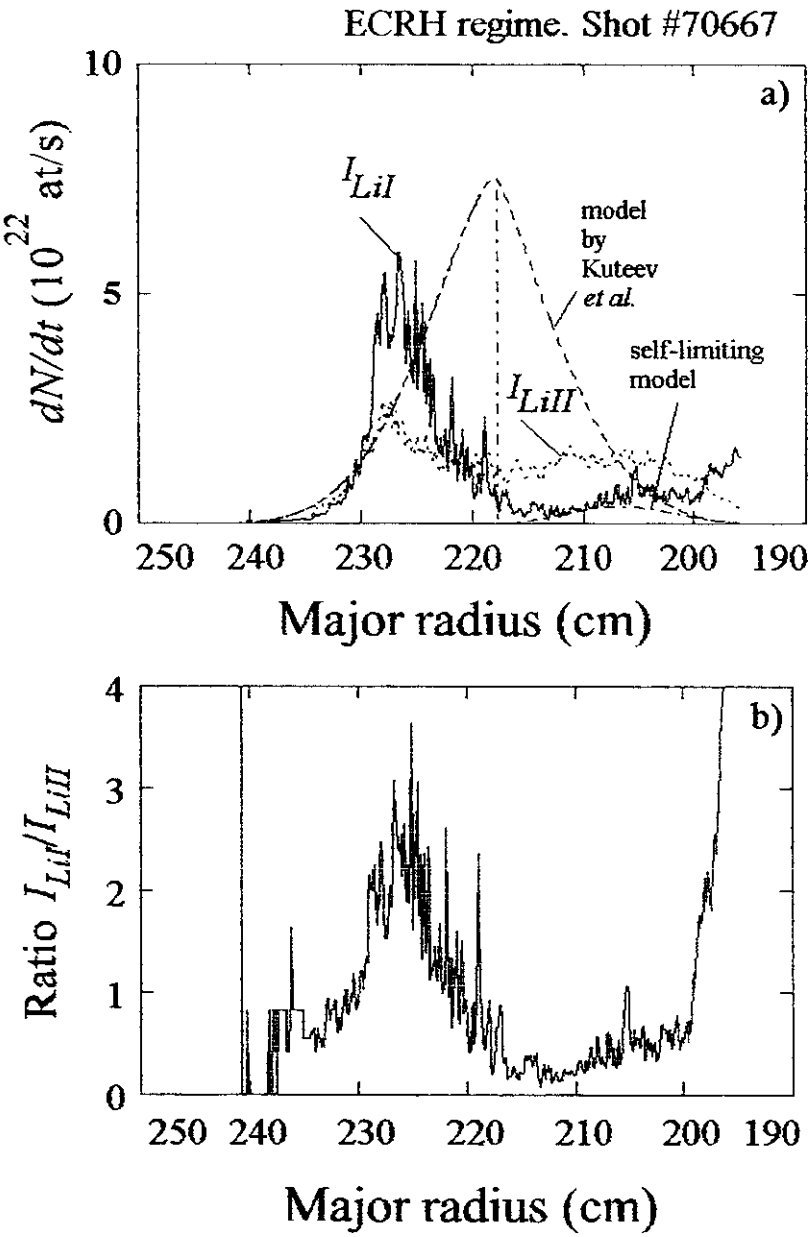
ECRH regime. Shot #70667
a)
I_{LiI}
model by Kuteev *et al.*
self-limiting model
I_{LiII}
dN/dt (10^{22} at/s)
Major radius (cm)
b)
Ratio I_{LiI}/I_{LiII}
Major radius (cm)

Fig. 8

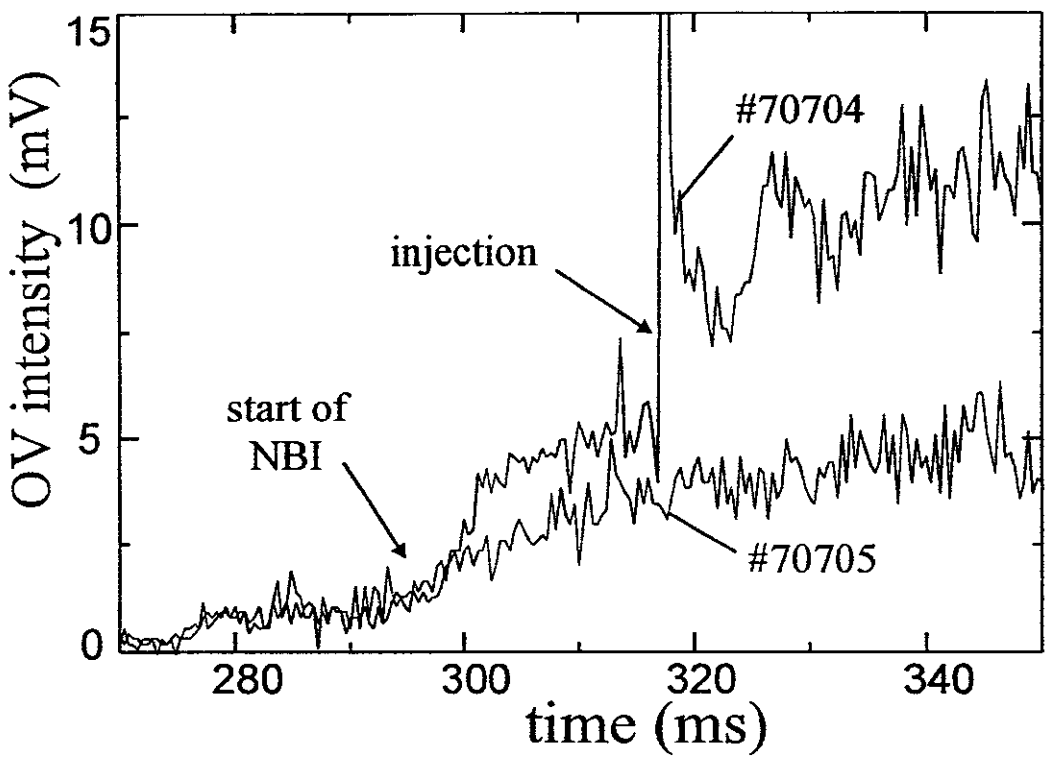
15
10
5
0
OV intensity (mV)
#70704
injection
start of
NBI
#70705
280
300
320
340
time (ms)

Fig. 9

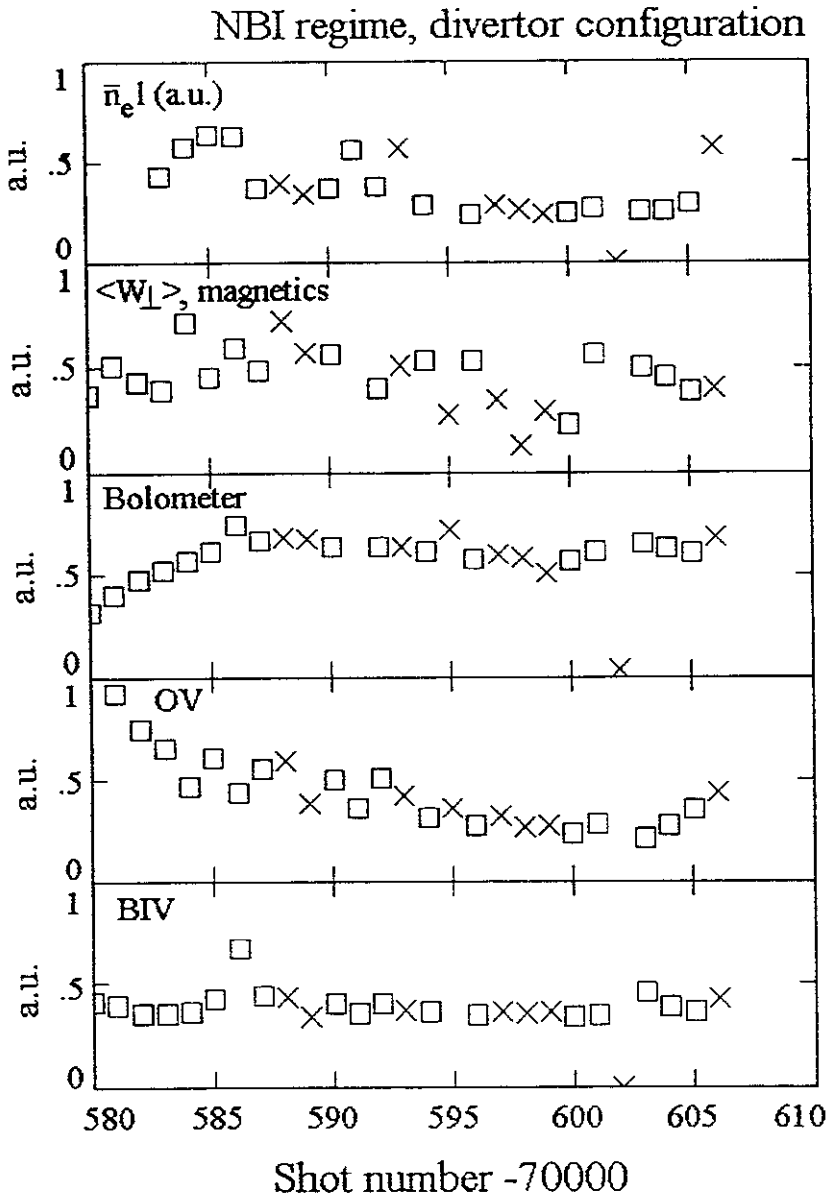
NBI regime, divertor configuration
$\bar{n}_e l$ (a.u.)
<$W_\perp$>, magnetics
Bolometer
OV
BIV
a.u.
1
.5
0
580
585
590
595
600
605
610
Shot number -70000

Fig. 10

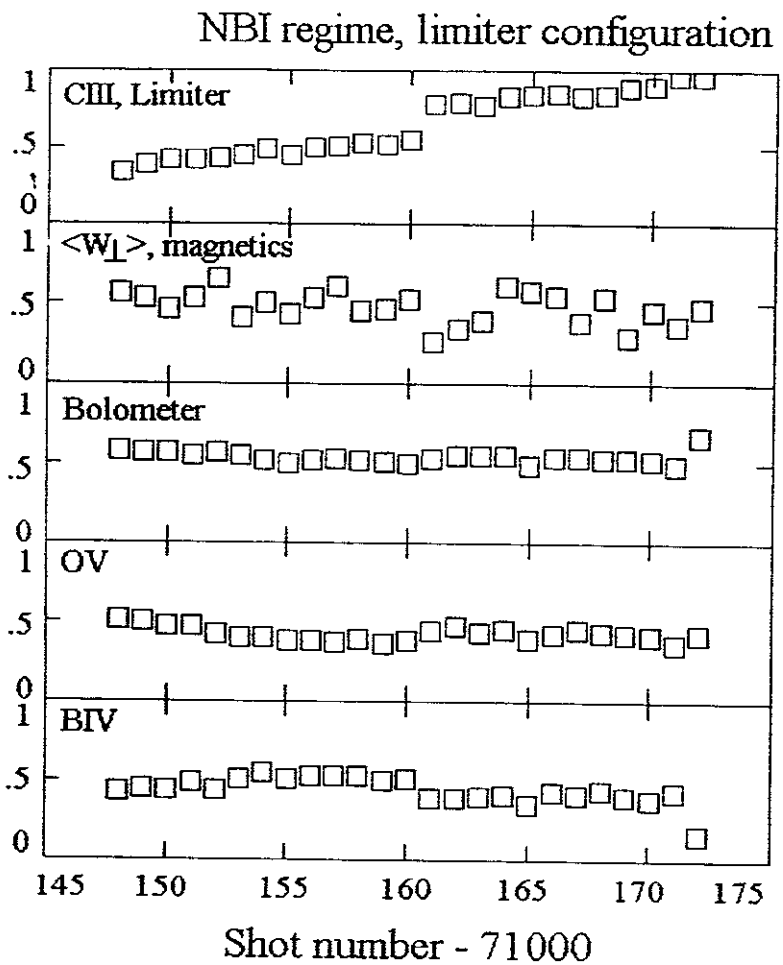
NBI regime, limiter configuration
CIII, Limiter
<W⊥>, magnetics
Bolometer
OV
BIV
1
.5
0
145
150
155
160
165
170
175
Shot number - 71000

Fig. 11

Recent Issues of NIFS Series

NIFS-383 K. Ichiguchi, O. Motojima, K. Yamazaki, N. Nakajima and M. Okamoto
Flexibility of LHD Configuration with Multi-Layer Helical Coils;
Nov. 1995

NIFS-384 D. Biskamp, E. Schwarz and J.F. Drake,
Two-dimensional Electron Magnetohydrodynamic Turbulence; Nov. 1995

NIFS-385 H. Kitabata, T. Hayashi, T. Sato and Complexity Simulation Group,
Impulsive Nature in Collisional Driven Reconnection; Nov. 1995

NIFS-386 Y. Katoh, T. Muroga, A. Kohyama, R.E. Stoller, C. Namba and O. Motojima,
Rate Theory Modeling of Defect Evolution under Cascade Damage Conditions:The Influence of Vacancy-type Cascade Remnants and Application to the Defect Production Chracterization by Microstructural Analysis; Nov. 1995

NIFS-387 K. Araki, S. Yanase and J. Mizushima,
Symmetry Breaking by Differential Rotation and Saddle-node Bifurcation of the Thermal Convection in a Spherical Shell; Dec. 1995

NIFS-388 V.D. Pustovitov,
Control of Pfirsch-Schlüter Current by External Poloidal Magnetic Field in Conventional Stellarators: Dec. 1995

NIFS-389 K. Akaishi,
On the Outgassing Rate Versus Time Characteristics in the Pump-down of an Unbaked Vacuum System; Dec. 1995

NIFS-390 K.N. Sato, S. Murakami, N. Nakajima, K. Itoh,
Possibility of Simulation Experiments for Fast Particle Physics in Large Helical Device (LHD); Dec. 1995

NIFS-391 W.X.Wang, M. Okamoto, N. Nakajima, S. Murakami and N. Ohyabu,
A Monte Carlo Simulation Model for the Steady-State Plasma in the Scrape-off Layer; Dec. 1995

NIFS-392 Shao-ping Zhu, R. Horiuchi, T. Sato and The Complexity Simulation Group,
Self-organization Process of a Magnetohydrodynamic Plasma in the Presence of Thermal Conduction; Dec. 1995

NIFS-393 M. Ozaki, T. Sato, R. Horiuchi and the Complexity Simulation Group
Electromagnetic Instability and Anomalous Resistivity in a Magnetic Neutral Sheet; Dec. 1995

NIFS-394 K. Itoh, S.-I Itoh, M. Yagi and A. Fukuyama,
Subcritical Excitation of Plasma Turbulence; Jan. 1996

NIFS-395 H. Sugama and M. Okamoto, W. Horton and M. Wakatani,
Transport Processes and Entropy Production in Toroidal Plasmas with Gyrokinetic Eletromagnetic Turbulence; Jan. 1996

NIFS-396 T. Kato, T. Fujiwara and Y. Hanaoka,
X-ray Spectral Analysis of Yohkoh BCS Data on Sep. 6 1992 Flares - Blue Shift Component and Ion Abundances -; Feb. 1996

NIFS-397 H. Kuramoto, N. Hiraki, S. Moriyama, K. Toi, K. Sato, K. Narihara, A. Ejiri, T. Seki and JIPP T-IIU Group,
Measurement of the Poloidal Magnetic Field Profile with High Time Resolution Zeeman Polarimeter in the JIPP T-IIU Tokamak; Feb. 1996

NIFS-398 J.F. Wang, T. Amano, Y. Ogawa, N. Inoue,
Simulation of Burning Plasma Dynamics in ITER; Feb. 1996

NIFS-399 K. Itoh, S-I. Itoh, A. Fukuyama and M. Yagi,
Theory of Self-Sustained Turbulence in Confined Plasmas; Feb. 1996

NIFS-400 J. Uramoto,
A Detection Method of Negative Pionlike Particles from a H2 Gas Descharge Plasma; Feb. 1996

NIFS-401 K.Ida, J.Xu, K.N.Sato, H.Sakakita and JIPP TII-U group,
Fast Charge Exchange Spectroscopy Using a Fabry-Perot Spectrometer in the JIPP TII-U Tokamak; Feb. 1996

NIFS-402 T. Amano,
Passive Shut-Down of ITER Plasma by Be Evaporation; Feb. 1996

NIFS-403 K. Orito,
A New Variable Transformation Technique for the Nonlinear Drift Vortex; Feb. 1996

NIFS-404 T. Oike, K. Kitachi, S. Ohdachi, K. Toi, S. Sakakibara, S. Morita, T. Morisaki, H. Suzuki, S. Okamura, K. Matsuoka and CHS group; *Measurement of Magnetic Field Fluctuations near Plasma Edge with Movable Magnetic Probe Array in the CHS Heliotron/Torsatron*; Mar. 1996

NIFS-405 S.K. Guharay, K. Tsumori, M. Hamabe, Y. Takeiri, O. Kaneko, T. Kuroda,
Simple Emittance Measurement of H- Beams from a Large Plasma Source; Mar. 1996

NIFS-406 M. Tanaka and D. Biskamp,
Symmetry-Breaking due to Parallel Electron Motion and Resultant Scaling in Collisionless Magnetic Reconnection; Mar. 1996

NIFS-407 K. Kitachi, T. Oike, S. Ohdachi, K. Toi, R. Akiyama, A. Ejiri, Y. Hamada,

H.Kuramoto, K. Narihara, T. Seki and JIPP T-IIU Group,
Measurement of Magnetic Field Fluctuations within Last Closed Flux Surface with Movable Magnetic Probe Array in the JIPP T-IIU Tokamak; Mar. 1996

NIFS-408 K. Hirose. S. Saito and Yoshi.H. Ichikawa
Structure of Period-2 Step-1 Accelerator Island in Area Preserving Maps; Mar. 1996

NIFS-409 G.Y.Yu, M. Okamoto, H. Sanuki, T. Amano,
Effect of Plasma Inertia on Vertical Displacement Instability in Tokamaks; Mar. 1996

NIFS-410 T. Yamagishi,
Solution of Initial Value Problem of Gyro-Kinetic Equation; Mar. 1996

NIFS-411 K. Ida and N. Nakajima,
Comparison of Parallel Viscosity with Neoclassical Theory; Apr. 1996

NIFS-412 T. Ohkawa and H. Ohkawa,
Cuspher. A Combined Confinement System; Apr. 1996

NIFS-413 Y. Nomura, Y.H. Ichikawa and A.T. Filippov,
Stochasticity in the Josephson Map; Apr. 1996

NIFS-414 J. Uramoto,
Production Mechanism of Negative Pionlike Particles in H_2 Gas Discharge Plasma; Apr. 1996

NIFS-415 A. Fujisawa, H. Iguchi, S. Lee, T.P. Crowley, Y. Hamada, S. Hidekuma, M. Kojima,
Active Trajectory Control for a Heavy Ion Beam Probe on the Compact Helical System; May 1996

NIFS-416 M. Iwase. K. Ohkubo, S. Kubo and H. Idei
Band Rejection Filter for Measurement of Electron Cyclotron Emission during Electron Cyclotron Heating; May 1996

NIFS-417 T. Yabe, H. Daido,T. Aoki, E. Matsunaga and K. Arisawa,
Anomalous Crater Formation in Pulsed-Laser-Illuminated Aluminum Slab and Debris Distribution; May 1996

NIFS-418 J. Uramoto,
Extraction of K^- Mesonlike Particles from a D_2 Gas Discharge Plasma in Magnetic Field; May 1996

NIFS-419 J. Xu, K. Toi, H. Kuramoto, A. Nishizawa, J. Fujita, A. Ejiri, K. Narihara, T. Seki, H. Sakakita, K. Kawahata, K. Ida, K. Adachi, R. Akiyama, Y. Hamada,

S. Hirokura, Y. Kawasumi, M. Kojima, I. Nomura, S. Ohdachi, K.N. Sato
Measurement of Internal Magnetic Field with Motional Stark Polarimetry in Current Ramp-Up Experiments of JIPP T-IIU; June 1996

NIFS-420 Y.N. Nejoh,
Arbitrary Amplitude Ion-acoustic Waves in a Relativistic Electron-beam Plasma System; July 1996

NIFS-421 K. Kondo, K. Ida, C. Christou, V.Yu.Sergeev, K.V.Khlopenkov, S.Sudo, F. Sano, H. Zushi, T. Mizuuchi, S. Besshou, H. Okada, K. Nagasaki, K. Sakamoto, Y. Kurimoto, H. Funaba, T. Hamada, T. Kinoshita, S. Kado, Y. Kanda, T. Okamoto, M. Wakatani and T. Obiki,
Behavior of Pellet Injected Li Ions into Heliotron E Plasmas; July 1996

NIFS-422 Y. Kondoh, M. Yamaguchi and K. Yokozuka,
Simulations of Toroidal Current Drive without External Magnetic Helicity Injection: July 1996

NIFS-423 Joong-San Koog,
Development of an Imaging VUV Monochromator in Normal Incidence Region: July 1996

NIFS-424 K. Orito,
A New Technique Based on the Transformation of Variables for Nonlinear Drift and Rossby Vortices; July 1996

NIFS-425 A. Fujisawa, H. Iguchi, S. Lee, T.P. Crowley, Y. Hamada, H. Sanuki, K. Itoh, S. Kubo, H. Idei, T. Minami, K. Tanaka, K. Ida, S. Nishimura, S. Hidekuma, M. Kojima, C. Takahashi, S. Okamura and K. Matsuoka,
Direct Observation of Potential Profiles with a 200keV Heavy Ion Beam Probe and Evaluation of Loss Cone Structure in Toroidal Helical Plasmas on the Compact Helical System; July 1996

NIFS-426 H. Kitauchi, K. Araki and S. Kida,
Flow Structure of Thermal Convection in a Rotating Spherical Shell; July 1996

NIFS-427 S. Kida and S. Goto,
Lagrangian Direct-interaction Approximation for Homogeneous Isotropic Turbulence; July 1996

NIFS-428 V.Yu. Sergeev, K.V. Khlopenkov, B.V. Kuteev, S. Sudo, K. Kondo, F. Sano, H. Zushi, H. Okada, S. Besshou, T. Mizuuchi, K. Nagasaki, Y. Kurimoto and T. Obiki,
Recent Experiments on Li Pellet Injection into Heliotron E; Aug. 1996